

## Article

# Land Cover Classification by Gaofen Satellite Images Based on CART Algorithm in Yuli County, Xinjiang, China

Chunyu Li <sup>1,2,3</sup>, Rong Cai <sup>1,2,\*</sup>, Wei Tian <sup>1</sup>, Junna Yuan <sup>1</sup> and Xiaofei Mi <sup>1</sup><sup>1</sup> Aerospace Information Research Institute, Chinese Academy of Sciences, Beijing 100094, China<sup>2</sup> School of Aeronautics and Astronautics, University of Chinese Academy of Sciences, Beijing 100049, China<sup>3</sup> Investigation College of People's Public Security University of China, Beijing 100038, China

\* Correspondence: cairong@aircas.ac.cn

**Abstract:** High-resolution remote-sensing images can be used in human activity analysis and criminal activity monitoring, especially in sparsely populated zones. In this paper, we explore the applicability of China's Gaofen satellite images in the land cover classification of Xinjiang, China. First of all, the features of spectral reflectance and a normalized radar cross section (NRCS) for different types of land covers were analyzed. Moreover, the seasonal variation of the NRCS in SAR (Synthetic Aperture Radar) images for the study area, Dunkuotan Village of Yuli County, China, was demonstrated by the GEE (Google Earth Engine) platform accordingly. Finally, the CART (classification and regression trees) algorithm of a DT (decision tree) was applied to investigate the classification of land cover in the western area of China when both optical and SAR images were employed. An overall classification accuracy of 83.15% with a kappa coefficient of 0.803 was observed by using GF-2/GF-3 images (2017–2021) in the study area. The DT-based classification procedure proposed in this investigation proved that Gaofen series remote-sensing images can be engaged to effectively promote the routine workflow of the administrative department.

**Keywords:** land cover; classification; Gaofen satellite; Google Earth Engine; CART; decision tree; Xinjiang



**Citation:** Li, C.; Cai, R.; Tian, W.; Yuan, J.; Mi, X. Land Cover Classification by Gaofen Satellite Images Based on CART Algorithm in Yuli County, Xinjiang, China. *Sustainability* **2023**, *15*, 2535. <https://doi.org/10.3390/su15032535>

Academic Editor: Xia Min

Received: 9 November 2022

Revised: 18 January 2023

Accepted: 20 January 2023

Published: 31 January 2023



**Copyright:** © 2023 by the authors. Licensee MDPI, Basel, Switzerland. This article is an open access article distributed under the terms and conditions of the Creative Commons Attribution (CC BY) license (<https://creativecommons.org/licenses/by/4.0/>).

## 1. Introduction

### 1.1. Remote-Sensing Big Data

As satellite remote-sensing (RS) technology has developed, the spatial and temporal resolution of satellite images has significantly improved over the past two decades. The intelligent applications of remote-sensing big data, therefore, are bound to be researched and developed, which aim to provide scientific big data and decision-making assistance for supporting sustainable social and economic development while building a community with a shared future for humankind [1].

Spatial information is of essentially importance for the sustainable administration of government, while remote-sensing big data are able to be used in the investigation and monitoring of national territory resources and security because they are characterized by wide coverage, high resolution and user privacy [2]. Moreover, remote-sensing big data could also effectively alleviate the difficulties of manual information collection and acquisition and promote the updating and integrating of background information. Finally, the combination of high-resolution remote-sensing images, global navigation and positioning (GPS) technology and geographic information systems (GISs) could implement the efficient reconnaissance and dynamic trajectory analysis of criminal activity, especially in sparsely populated regions, the west of China, for example.

When Albert Gore, former vice president of the United States, proposed “big data for the earth”, satellite remote sensing was entering the era of big data [3]. Since the successful launch of the first US meteorological satellite in 1960, there have been 558 earth observation satellites launched, as of September 2020 [4]. China, for instance, has more than

500 satellites in orbit, as of 24 April 2022. How remote-sensing data can be accurately, fast and intelligently gathered and how the information coming from remote-sensing satellite big data can be mined are the core issues with the application of big data of remote-sensing satellites [5].

In the past decade, remote-sensing big data platforms, such as the Google Earth Engine (GEE) [6], NEX (NASA Earth exchange), Descartes Labs, Amazon Web Services (AWS), Data Cube of Australia and CODE-DE (Copernicus Data and Exploitation Platform-DE) from Germany, etc., have rapidly developed and achieved many typical applications [7–9].

China's remote-sensing cloud-computing platform is also rapidly developing. For example, the Earth Data Miner [10] supported by the pilot project "Earth Big Data Science Project", run by the Chinese Academy of Sciences, and Pixel Information Expert (PIE), a cloud computation platform of PIESAT Group Inc., are representative remote sensing big data platforms in early development. In addition, Alibaba cloud, Tencent cloud and the Sense Earth platforms of SenseTime Group Inc. have also play a leading role in terms of remote-sensing cloud computing in China. Remote-sensing cloud-computing platforms make the real-time processing of massive satellite remote-sensing big data possible and have been industrialized in many fields, such as earth science, GISs, disaster prevention and mitigation, emergency rescue and even public security.

With the advent of the era of big data, deep learning models represented by decision trees, random forests, convolutional neural networks, etc. have been widely used in the field of remote sensing. A large number of remote-sensing data sets has been produced and released, such as UC Merced, WHU-RS19, Gaofen Image Datasets (GIDs), etc., over the past few years, and those data sets have been successfully applied in neural net optimization and prediction algorithm improvement [11]. As deep learning models require massive samples to be trained and tested, the demand for high-resolution remotely sensed image data sets has exploded, which has been enhanced by the rapid development of the big data of remote sensing, parallel computing and artificial intelligence. The remote-sensing data set, including onsite pictures, attribute information, etc., are vital for model training and algorithm testing in regard to the process of machine learning for many research fields of remote-sensing applications, such as target recognition, land cover and land utilization classification [12].

### 1.2. China's Gaofen Satellite Constellation

China's High-Resolution Earth Observation System (CHEOS) was approved in 2010 by the Chinese government. It consists of a space-based observation system, a near-space observation system, an aviation observation system, a ground system and an application system. Seven civil satellites have been successfully launched so far, which are named after Gaofen (GF). The Gaofen satellite constellation combines the advantages of high temporal resolution and high spatial resolution. Various sensors are deployed on the Gaofen series satellites.

The GF-1 satellite carries two panchromatic multispectral cameras (PMS, 2 m for PAN and 8 m for MS) and four wide-field-of-view (WFV) cameras with a resolution of 16 m. The GF-1 satellite is used mainly in public security, disaster prevention and urban land surveys. The sensor resolution on the GF-2 satellite is higher than that of the GF-1 satellite, with a resolution of 1 m for PAN and 4 m for MS. The GF-2 satellite can be used in high-precision land-use surveys, public security, reconnaissance and other application fields. The GF-3 is equipped with a C-band multipolarization synthetic aperture radar (SAR), 12 imaging modes and a spatial resolution of up to 1 m. The satellite payload can work under any weather conditions, day or night, because the electromagnetic waves (EMWs) radiated from the SAR sensor can penetrate clouds, surface vegetation, loose sand and even snow. The GF-3 satellite is widely used in marine protection, early-warning disaster-risk prevention and forecasting, water resource management and weather forecasting. The payloads and mission objectives of the Gaofen series satellites are shown in Table 1 [13].

**Table 1.** The payload and mission of the Gaofen satellite constellation of China.

Satellite	Date of Launch	Sensors	Missions
GF-1	26 April 2013	2 panchromatic multispectral cameras (2 m for panchromatic, 8 m for multispectral); 4 multispectral wide-width cameras (16 m)	Land resources and agricultural meteorology
GF-2	19 August 2014	2 panchromatic multispectral cameras (1 m for panchromatic, 4 m for multispectral)	Land and resources, urban management, transportation Marine application, disaster processing, water protection and
GF-3	10 August 2016	C-band multipolarization synthetic aperture radar (1~500 m)	management, meteorology prevention, mitigation of emergent disasters
GF-4	29 December 2015	Staring camera with visible (50 m) and near infrared (400 m)	Remote sensing of disaster reduction, forestry, meteorology
GF-5	9 May 2018	AHSI, VIMS, AIUS, EMI, GMI, DPC	Monitoring atmospheric aerosol, sulfur dioxide, nitrogen dioxide, methane, water quality, straw burning, urban heat island
GF-6	2 June 2018	1 panchromatic multispectral camera (2 m for panchromatic, 8 m for multispectral); 1 multispectral wide-width camera (16 m) A dual-linear array camera (back sight: 0.65 m, fore sight: 0.8 m); multispectral (back sight: 2.6 m); a laser altimeter (ranging accuracy $\leq 0.3$ m) (slope is less than 15 degrees); a footprint camera ( $\leq 4$ m)	Land resources, agricultural meteorology, identification of ground crops
GF-7	3 November 2019		Agricultural surveying and mapping of topography

### 1.3. Image Classification by Means of Machine Learning

A decision tree (DT) is one of the most intuitively effective classifiers applied in the automatic identification of remote-sensing images. CART is one of the DT classification algorithms, and it is widely used in machine learning and artificial intelligence [14–16]. CART is an intelligent algorithm that uses recursive segmentation technology to build a prediction model, which analyzes the relationship between multiple attributes and decisions to generate easy-to-understand rules for prediction [15–17]. The CART method is widely used in remote-sensing classification-based tasks, such as land cover mapping, forest remote-sensing surveys, crop area extraction, land desertification mapping, etc. [18,19]. The Gini coefficient is engaged in the measurement of the impurity of a given element with respect to the rest of the classes in CART [20,21]. Accordingly, by using a set of features, the maximum depth of the decision tree is reached.

The DT can be modeled as a set of if-then rules, which is applicable in categorical data. Once the model has been developed, classification is extremely quick because no further complex mathematics is required. Problems with DTs include the possibility of generating a nonoptimal solution and overfitting. The latter is normally addressed by pruning the tree, removing one or more layers of splits. Pruning reduces the accuracy of classifying the training data but generally increases the accuracy of dealing with unknowns [22].

In this study, a DT-based land cover classification was proposed by using Gaofen series satellite images, taking Yuli County, Xinjiang, China, as the study area. First of all, GF-2/GF-3 data were introduced, and a preprocessing procedure was demonstrated. Next, various features of optical and SAR images were investigated, and a multiseasonal merged SAR image was displayed. In addition, the CART algorithm of the decision tree was applied to train the classifier and to output the classification result. Finally, a case study of the DT-based classification was presented for Dunkuotan Village of Yuli County, and a classification accuracy assessment was proposed. The supervised classification scheme

proposed in this paper could effectively promote the routine administrative and supervised workflow when remote-sensing images are applied, according to our investigation.

## 2. Data and Methodology

### 2.1. Study Area

The study area of this paper is in Dunkuotan Village, Yuli County, Xinjiang Uygur Autonomous Region, China. Yuli County, also known as Lop Nur, is in the middle of Xinjiang, China (Figure 1). Yuli County is in the southern foothills of the Tianshan Mountains and on the northeast edge of the Tarim Basin. Dunkuotan Village is 24 km away from Yuli County, with a total area of 15,468.9 km<sup>2</sup> and an average altitude of 901 m. Dunkuotan Village is suitable as a research area of the Chinese western social economy and natural resources development because it is not only the geographical center of Xinjiang but also the intercontinental hub of the Silk Road Economic Belt.

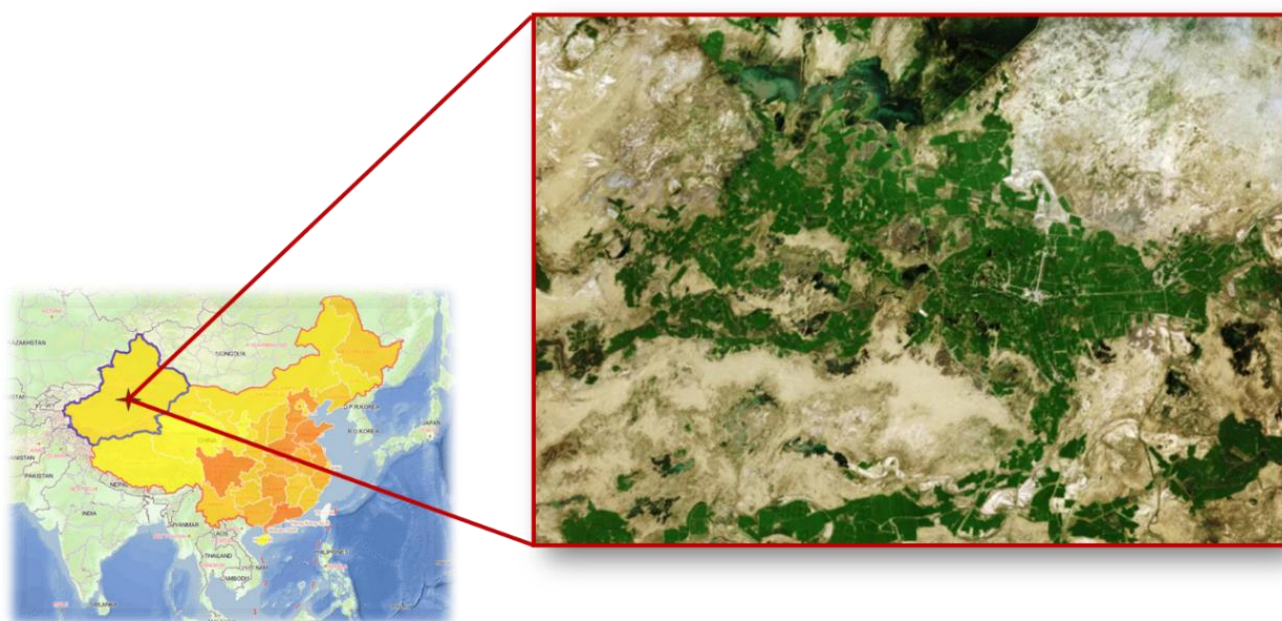


**Figure 1.** Map of the study area. The left map shows the location of Yuli County, Xinjiang, China, and the right picture is a remotely sensed image of a part of Dunkuotan Village, Yuli County.

The study area is located in the Asia–Africa desert region, with complicated plant composition and low vegetation coverage. The grassland in the study area is composed mainly of perennial tepid and xerophytic plants. Most of them are in the form of shrub grassland, which is short and sparse. The woodland vegetation, on the other hand, is composed mainly of sparse *Populus euphratica*. The shrubbery is red willow, with rich constructive species and diverse ecological types. The river net structure is determined by the topography in the study area. In addition, the simple road, around 6 m in width, is the common type of road. The rooftops are made up of either cement/metal (for most of the town area) or wood/cement (for the rural area), according to the onsite investigations (see Figure 2).



**Figure 2.** The onsite photos of the typical roads and buildings in the study area.

## 2.2. Data and Preprocessing

### 2.2.1. GF-2 Data and Preprocessing

In this investigation, 16 GF-2 images are collected, which are acquired in four seasons, ranging from 28 January 2017 to 22 December 2021 (see Table 2). Each GF-2 image in the L1A redistributed level consists of two types of data products: the panchromatic (1 m resolution) and the multispectral (4 m resolution) product, respectively. The high-resolution CCD sensor, mounted on a GF-2 satellite platform, works in four spectral bands (B1/blue: 0.45–0.52  $\mu\text{m}$ , B2/green: 0.52–0.59  $\mu\text{m}$ , B3/red: 0.63–0.69  $\mu\text{m}$  and B4/NIR: 0.77–0.89  $\mu\text{m}$ ), plus a panchromatic band (PAN: 0.45–0.90  $\mu\text{m}$ ), which is the same as that of the GF-1 satellite.

The preprocessing of GF-2 data includes radiation calibration, atmospheric correction, geometrical correction and image fusion. First, the radiation calibration procedure was implemented by using ENVI 5.3 software [23] by Harris Corporation in Melbourne, Florida, USA. In this phase, the pixel digital number (DN) in every band (B1–B4) of the GF-2 data was converted to the value of radiance to minimize the uncertainty produced by the CCD sensor. Next, the atmospheric correction was conducted by using the FLAASH (Fast Line-of-sight Atmospheric Analysis of Spectral Hypercubes) atmospheric correction toolbox in ENVI 5.3, such that the pixels in the four spectral bands were represented in the value of spectral reflectance. Thereafter, the RPC model-based geo-correction procedure was implemented by analyzing the rational polynomial coefficient (RPC) file, which is associated with the image files in the data package of the GF-2 data. Finally, the NNDiffuse Pan Sharpening toolbox in ENVI 5.3 software was utilized to improve the spatial resolution of a multispectral image from 4 m to 1 m.

**Table 2.** GF-2 data collected in this paper.

Platform	Sensor	Date of Acquisition	Number of Scenes	Spatial Resolution
GF-2	PMS1	28 January 2017	1	1 m/4 m
GF-2	PMS1	3 August 2017	1	1 m/4 m
GF-2	PMS1	26 October 2017	2	1 m/4 m
GF-2	PMS2	31 October 2017	1	1 m/4 m
GF-2	PMS1	9 December 2018	1	1 m/4 m
GF-2	PMS2	9 December 2018	1	1 m/4 m
GF-2	PMS2	16 September 2019	1	1 m/4 m
GF-2	PMS1	19 November 2019	2	1 m/4 m
GF-2	PMS2	15 February 2021	1	1 m/4 m
GF-2	PMS1	24 May 2021	2	1 m/4 m
GF-2	PMS2	14 October 2021	1	1 m/4 m
GF-2	PMS2	22 December 2021	1	1 m/4 m
GF-2	PMS2	1 March 2022	1	1 m/4 m

### 2.2.2. GF-3 Data and Preprocessing

The GF-3 SAR sensor is able to image in 12 modes. For instance, the spot light (SL) mode image has the highest spatial resolution, of up to 1 m, among all of the imaging modes, and the Quad-Polarization Strip I (QPSI) mode image has the most polarization channels (HH/HV/VH/VV), with a nominal spatial resolution of 8 m. In this investigation, 14 Ultra Fine Strip (UFS) mode GF-3 images were collected (Table 3), which have a relatively high spatial resolution (3 m) and wider swath (30 km), in HH polarization.

**Table 3.** GF-3 data collected in this paper.

Platform/Sensor	Date of Acquisition	Imaging Mode	Spatial Resolution	Polarization
GF-3/SAR	8 September 2018	UFS	3 m	HH
GF-3/SAR	8 April 2019	UFS	3 m	HH
GF-3/SAR	3 August 2019	UFS	3 m	HH
GF-3/SAR	16 June 2020	UFS	3 m	HH
GF-3/SAR	31 August 2020	UFS	3 m	HH
GF-3/SAR	30 September 2020	UFS	3 m	HH
GF-3/SAR	5 January 2021	UFS	3 m	HH
GF-3/SAR	4 March 2021	UFS	3 m	HH
GF-3/SAR	1 May 2021	UFS	3 m	HH
GF-3/SAR	28 June 2021	UFS	3 m	HH
GF-3/SAR	23 July 2021	UFS	3 m	HH
GF-3/SAR	18 October 2021	UFS	3 m	HH
GF-3/SAR	16 November 2021	UFS	3 m	HH
GF-3/SAR	10 April 2022	UFS	3 m	HH

A series of preprocessing procedures was performed on the single-look complex images using PIE-SAR 6.3 software [24] by PIESAT Information Technology Co., Ltd. First of all, the multilook module was applied to improve the quality of the single-look SAR image at the L1A processing level. Next, the enhanced frost filter, with a window size of 3 by 3 and damping ratio of 1, was applied to reduce the speckle noise. In addition, the geocoded terrain correction (GTC) module was implemented by using a DEM map around the study area. Finally, radiometric calibration was conducted to convert the DN value of the pixel into the normalized radar cross section (NRCS).

The overall preprocessing procedure was drawn in Figure 3.

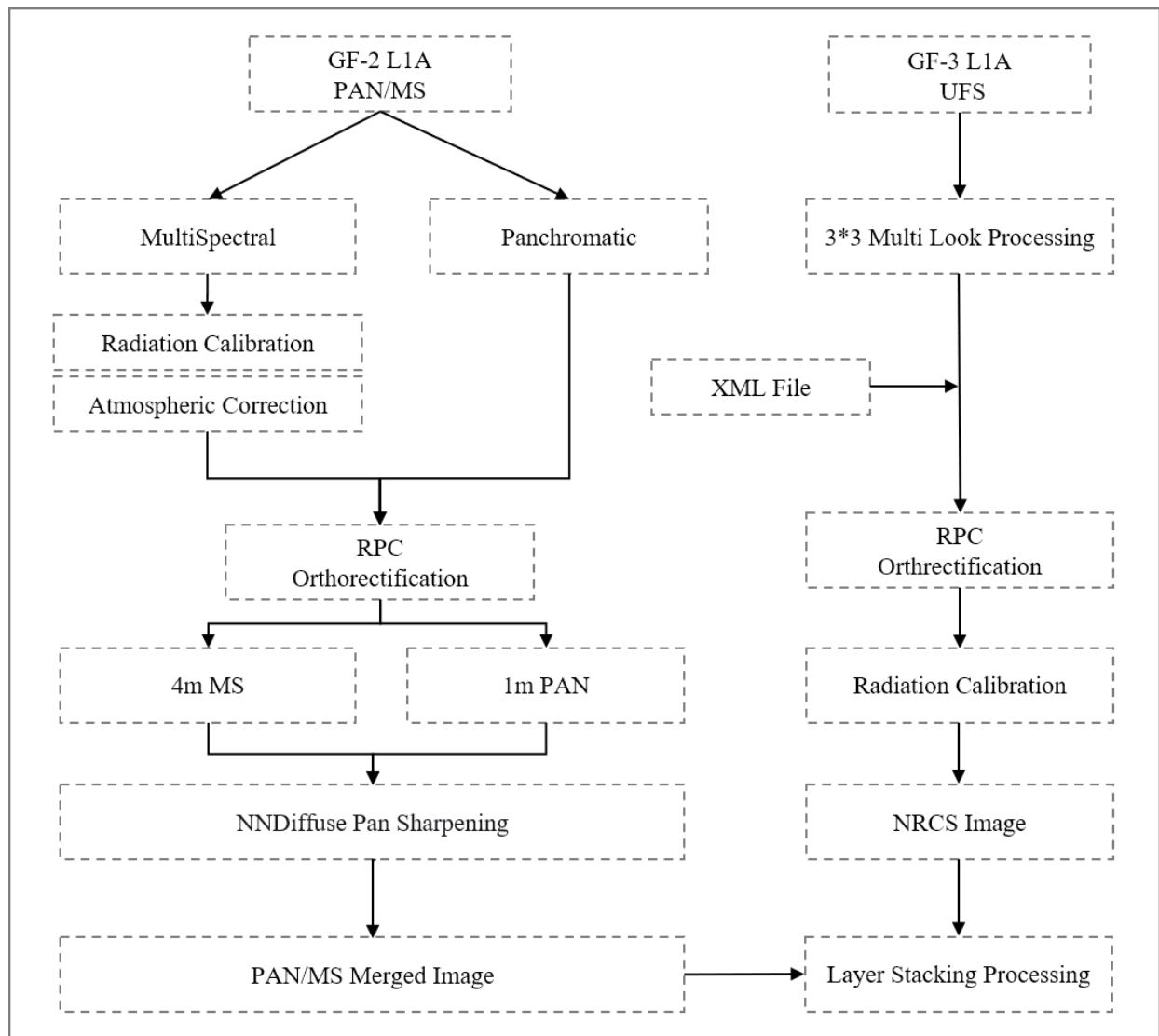


**Figure 3.** The flowchart of preprocessing for GF-2/GF-3 data.

### 2.3. Methodology

#### 2.3.1. Feature Extraction

Four kinds of features were extracted to discriminate between different types of land cover in the study area: spectral features, vegetation indexes, a water index and a radar backscattering coefficient. Four bands of GF-2 data were selected as the spectral features: blue, green, red and NIR. The normalized difference vegetation index (NDVI) and the enhanced vegetation index (EVI) served as the vegetation indexes. The normalized difference water index (NDWI) is the water index in this investigation. These indexes are defined as follows [25,26]:

$$NDVI = \frac{\rho_{NIR} - \rho_{red}}{\rho_{NIR} + \rho_{red}} \quad (1)$$

$$EVI = 2.5 \times \frac{\rho_{NIR} - \rho_{red}}{\rho_{NIR} + 6\rho_{red} - 7.5\rho_{blue} + 1} \quad (2)$$

$$NDWI = \frac{\rho_{green} - \rho_{NIR}}{\rho_{green} + \rho_{NIR}} \quad (3)$$

where  $\rho$  denotes the reflectance in different spectral bands: NIR, red, green or blue.

The NRCS, extracted from the calibrated GF-3 SAR image, on the other hand, can be used as the measurement of the radar backscattering from targets on the ground. The following equation [27] demonstrates the extraction of NRCS ( $\sigma_{dB}^0$ ) in the GF-3 product of L1A.

$$\sigma_{dB}^0 = 10 \times \lg \left[ P^I (QualifyValue / 32767)^2 \right] - K_{dB} \quad (4)$$

where  $P^I = I^2 + Q^2$  and  $I$  and  $Q$  are the real and imaginary parts of the GF-3 SAR data, respectively, in the product of L1A. The *QualifyValue* and  $K_{dB}$ , on the other hand, are constants that can be found in the field of *<QualifyValue>* and *<CalibrationConst>*, respectively, in the \*.meta.xml file of the GF-3 L1A product.

### 2.3.2. CART Method

The CART algorithm is able to divide n-dimensional space into nonoverlapping rectangles through recursion [28,29]. Let  $x_i$  be an independent variable; when  $x_i = u_i$ , the n-dimensional space is divided into two parts. Some points satisfy  $x_i \leq u_i$ , and the others satisfy  $x_i > u_i$ . For a discontinuous variable, there are only two values for the attribute value: equal or not equal. In the processing of recursion, these two parts reselect an attribute to a partition until the entire n-dimensional space is divided. Attributes with minimum Gini coefficient values are used as partition indexes. For a data set  $D$ , the Gini coefficient is defined as follows:

$$Gini(D) = 1 - \sum_k p_k^2 \quad (5)$$

where  $k$  is the number of categories of samples and  $p_k$  represents the probability that a sample will be classified as category  $k$ . The *Gini* coefficient indicates the degree of uncertainty that the samples in the data set belong to a certain category. The smaller the Gini coefficient, the smaller the uncertainty of the sample category, the higher is the purity of the sample, and thus the better the division effect is. If there is only one category in sample set  $D$ , the *Gini* coefficient will be 0 and the uncertainty of the sample category will be 0.

### 2.3.3. Evaluation Metrics

We use several widely adopted metrics [30,31], such as the producer's accuracy (PA), the user's accuracy (UA), the overall accuracy (OA) and the Kappa coefficient (Kappa), to quantitatively assess the accuracy of the classification in this paper, based on the resulting confusion matrix (Table 4)

$$PA = \frac{P_{j,j}}{\sum_{i=1}^n P_{i,j}} \quad (6)$$

$$UA = \frac{P_{i,i}}{\sum_{j=1}^n P_{i,j}} \quad (7)$$

$$OA = \frac{\sum_{i=1}^n P_{i,i}}{T} \quad (8)$$

$$Kappa = \frac{T \sum_{i=1}^n P_{i,i} - \sum_{i=1}^n (P_{i.} \times P_{.i})}{T^2 - \sum_{i=1}^n (P_{i.} \times P_{.i})} \quad (9)$$

where  $j$  is the  $j^{\text{th}}$  category of the predicted results,  $i$  is the  $i^{\text{th}}$  category of the validated results,  $T$  is the overall number of samples, and  $P_{i.}$  and  $P_{.i}$  are the sum of the samples in the  $i^{\text{th}}$  row and the  $i^{\text{th}}$  column in the confusion matrix, respectively.

**Table 4.** The confusion matrix.

		Validated Results			
		Category 1	Category 2	... ..	Category N
Predicted Results	Category 1	$p_{11}$	$p_{12}$	... ..	$p_{1N}$
	Category 2	$p_{21}$	$p_{22}$	... ..	$p_{2N}$
	... ..	... ..	... ..	... ..	... ..
	Category N	$p_{N1}$	$p_{N2}$	... ..	$p_{NN}$

### 3. Results and Discussions

#### 3.1. Spectral Feature Analysis

In the study area, the most common land cover types are vegetation, crops, bare soil (Gobi), desert, river, building, road and other. First of all, we analyzed the spectral features (Figure 4) of seven types of objects on the ground in the GF-2 multispectral image (Figure 5), which was acquired on 24 May 2021.

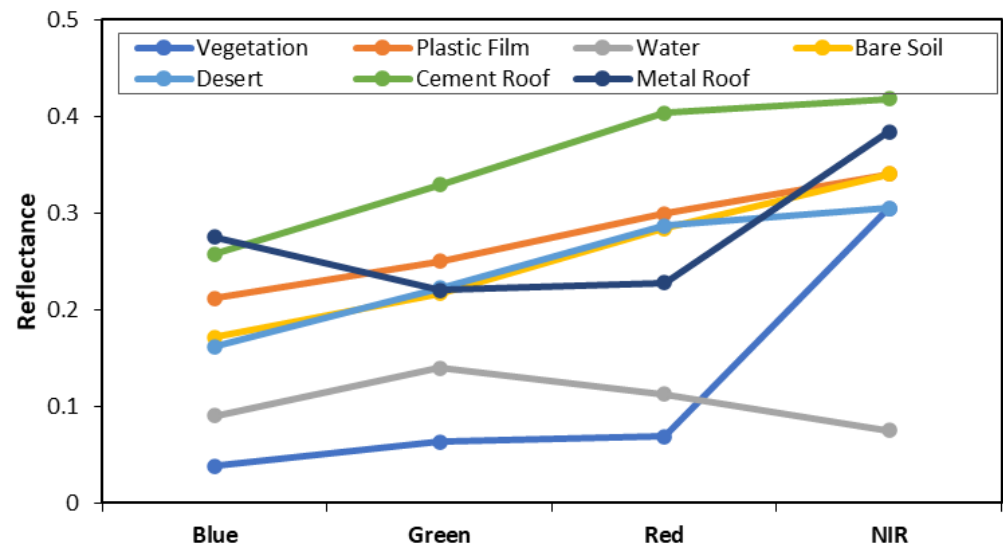


**Figure 4.** Mean reflectance of six types of samples extracted from GF-2 multispectral bands. Vegetation: land covered by vegetation; plastic film: land covered by plastic films; water: river, pool, lake, etc.; bare soil: land with no covers; desert: the desert samples; cement roof: rooftop that is made up of cement or similar materials; metal roof: rooftop that is made up of metal.

As shown in Figure 4, most of the samples are observed to have the highest reflectance in the NIR band, except water, which is able to absorb the NIR radiation to an extreme degree. It can be inferred that the water body can be identified by the reflectance of the NIR band or by the NDWI index instead. In addition, the samples of the cement rooftop show stronger reflectance in all of the four visible bands other than that of the metal rooftop or the land (either with covers or without). This interprets the rooftop of cement (mostly for the residential housing) as a bright rectangle in either the RGB composite or the pseudocolored imageries. The metal rooftop, on the other hand, shows the highest reflectance in the blue band, causing the rooftop to often be painted as blue. This kind of rooftop is often related to the factories or commercial buildings in Western China. In this paper, we introduce an index that identifies the feature of colored metal rooftops in accordance with the spectral reflectance (Figure 4), named the NDMRI (normalized difference metal rooftop index), which is defined as follows:

$$NDMRI = \frac{\rho_{blue} - \rho_{red}}{\rho_{blue} + \rho_{red}} \quad (10)$$

From Figure 5, we find that the water body and the buildings with the blue metal roof are highlighted in the NDWI and NDMRI image, respectively. Moreover, we are able to

discriminate between the metal and cement rooftop by the difference of spectral reflectance in red or green (see Figure 4). Accordingly, we analyze the ability of the feature extraction of NDVI and EVI regarding the different land cover types: crops, plastic film, desert and shrubs in the Gobi area (see Figure 6 for details).

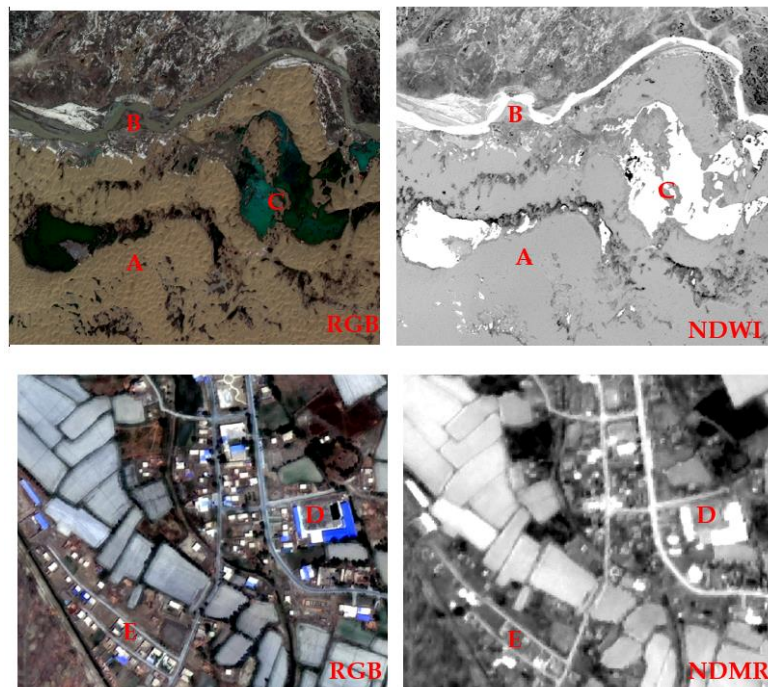


**Figure 5.** The GF-2 multispectral image slices (left), acquired on 24 May 2021, and the feature index image pairs (right). A: desert; B: river; C lake; D: blue metal rooftop of buildings; E: cement rooftop of buildings (white square).

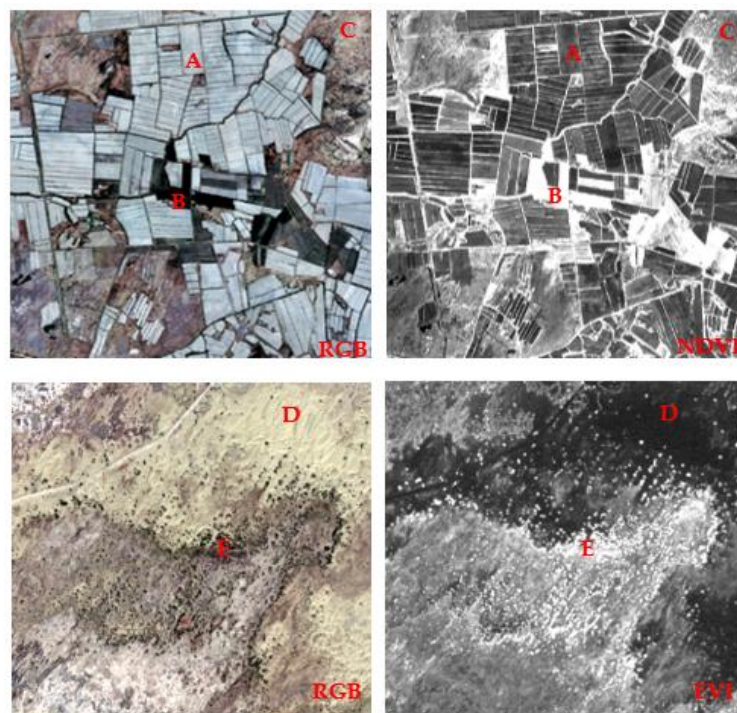


**Figure 6.** The GF-2 multispectral image slices (left), acquired on 24 May 2021, and the feature index image pairs (right). A: land covered by plastic film; B: land with vegetation/crops; C bare soil; D: desert; E: shrubs in the desert.

As shown in Figure 6, the NDVI index can be used to differentiate between land covered with plastic film (a common agricultural technique in the spring in Western China, serving to maintain the temperature and humidity of the soil below) and vegetation (crops). This is because the vegetation tends to reflect more NIR radiation than the agricultural plastic film. The EVI index, on the other hand, is shown as an effective indicator in identifying shrubs (brighter spot) from the Gobi Desert background (dark area of vegetation-free zone) (see the bottom left slice in Figure 6).

### 3.2. Radar Feature Analysis

The synthetic aperture radar (SAR) is a useful spaceborne sensor in various remote-sensing application aspects, such as natural resource monitoring, crop production assessment and ground object identification [32–35]. In this investigation, we analyze a set of features by using GF-3 SAR images so as to enhance the robustness of the trained classification model and diversify the type and number of remote-sensing data in the study area.

Figure 7 shows a pair of slices in the study area comparing GF-3 SAR imagery and GF-2 MS imagery. Four types of samples are assigned letters A–D. It was shown that SAR recognizes higher biomass (spot A) under the plastic film than the camera on board the GF-2 satellite, because of the penetrating ability of the microwave from using the SAR sensor. In other words, the electromagnetic waves of the SAR could detect the earth in cases where a thin plastic film is placed. Spot B shows a higher NDVI feature index yet is interpreted as a smaller NRCS (i.e., radar backscattering coefficient) value than that of spot A, which shows a lower NDVI index. This example implies that SAR imagery is a useful data set to identify land cover. Spots C and D, on the other hand, produced images with lower backscattering samples, resulting from the small surface roughness of bare soil, including those growing shrubbery.

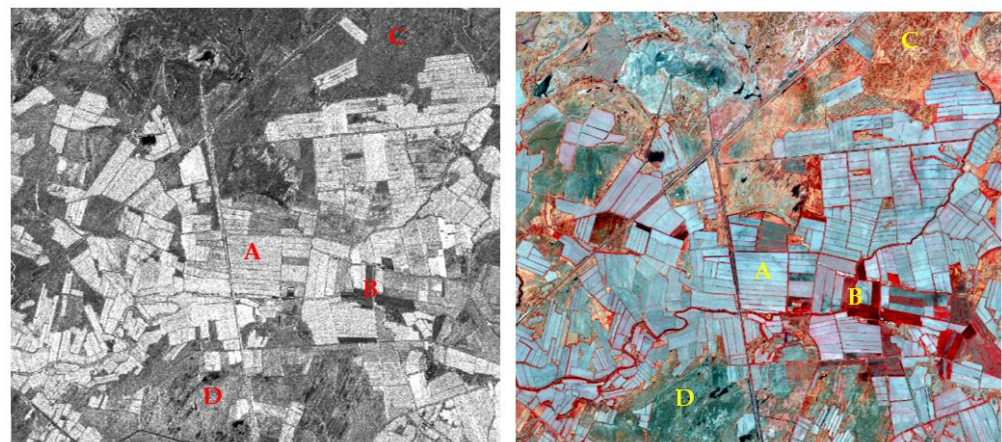


**Figure 7.** GF-3 SAR image of Dunkuotan Village (**left**), which was acquired on 28 June 2021 (in HH polarization, 3 m), and the GF-2 multispectral image pair (**right**), which was acquired on 24 May 2021 (R/G/B: NIR/red/green or band 4/3/2). A: land covered with higher biomass (vegetation); B: land covered with lower biomass (vegetation); C: bare soil covered by medium biomass (shrubs); D: bare soil covered by lower biomass (Gobi).

We summarize the radar features of five typical types of samples extracted from GF-3 SAR images (UFS) collected in this investigation (Table 5). As shown in Table 5, the difference between typical land covers can be drawn by MVN features. The highest value of NRCS in dB is observed for building,  $-1.33$  dB on average. However, this statistic should be recognized as the radar backscattering of the entire building rather than of the rooftop only, which dominates the spectral reflectance of pixels in GF-2 multispectral images. The reason is that the structural parameters, such as the shape and material of the rooftop, the location of scattering center, etc., determine the NRCS of a building. The lowest value of NRCS in dB, on the other hand, is observed for water, at  $-26.43$  dB on average, with a small

SDN of 1.23 dB. The desert is detected as a dark area in the C-band SAR images because the dryer the object is, the lower the signal backscattered is. We can see that the averaged NRCS for the desert is  $-21.69$  dB, half of that of bare soil, which is covered by rock, clay or salt crust in the study area. The vegetation, shown as bright spot in SAR images, is identified as  $-7.95$  dB of NRCS, resulting from the large biomass, as expected in summer.

**Table 5.** The statistical value of radar backscattering coefficient from GF-3 SAR images.

Features	Category				
	Vegetation	Bare Soil	Desert	Water	Building
Mean Value of NRCS (MVN, dB)	$-7.95$	$-12.88$	$-21.69$	$-26.43$	$-1.33$
Standard Deviation of NRCS (SDN, dB)	1.3	1.79	5.88	1.23	6.78

To demonstrate the seasonally varied characteristics of NRCS in SAR images, we produced a pseudo-colored SAR image (Figure 8) from multitemporal Sentinel-1 SAR data by the GEE platform (<https://earthengine.google.com/>, accessed on 30 December 2022). From Figure 8, we can see the image showed stronger brightness in the green band, which is related to the SAR image acquired in June, when higher biomass is expected than that in spring or winter. In addition, we can see the color changed among the cultivated lands in the study area. This is because the seasonal variation of NRCS is observed. Moreover, many extreme bright spots are displayed in Figure 8. These spots are related to the buildings that intensively reflect the incidence electromagnetic waves. It can be inferred from Figure 8 that SAR image bands can be used to improve the classification of land covers, in comparison with using the spectral bands of an image alone.



**Figure 8.** RGB composite map of Sentinel-1 SAR images (10 m, in VV polarization) of the study area, which was produced by the Google Earth Engine (GEE). R, G, B: the monthly averaged NRCS value of images taken in February, June and November of 2020, respectively.

It is interpreted from Figure 8 that mainly three types of land cover can be classified. Region A, which was shown as green patches in Figure 8, exhibited the highest backscattered power in June. This is because the shrubs in the Gobi Desert grow stronger in the summer than in the winter (channel B) or fall (channel R). Accordingly, region B, which is shown as bright yellow patches in Figure 8, is revealed as vegetation because of high backscattering in both channel R (SAR image acquired in Feb) and channel G (SAR images acquired in June). This is because the biomass of vegetation stays relatively high from spring through summer in the study area. Region C is interpreted as the center of Dunkuotan Village because the dense white spots are shown. This is because the residential buildings are proved to backscatter high in the SAR image throughout the year; i.e., there is no seasonal variance found between winter and summer for buildings in the SAR images. SAR images are verified to improve the detectability of buildings and many types of land cover, in comparison with when optical images are deployed only.

### 3.3. Classification Result of Decision Tree

#### 3.3.1. Rule Generation of CART

In this paper, the CART Rule Generator toolbox embedded in ENVI 5.3 was set to produce the rule for decision tree classification. Nine features discussed in this investigation, i.e., four spectral features, NDVI, EVI, NDWI, NDMRI, plus the radar backscattering coefficient, were input into the training procedure.

To obtain training samples for the classification and validation samples for an accuracy assessment, 280 photos taken from an onsite investigation and recorded with coordinates, along with the high-resolution GF-2 RGB composite images with varied acquisition time, were applied to manually recognize samples. All samples were randomly divided as 70% and 30% for training and validation, respectively.

#### 3.3.2. Accuracy Assessment

Table 6 shows the classification accuracy of the common objects in spring/summer (images from May/June 2021) of the study area computed by the confusion matrix. The overall accuracy is 83.15% with a kappa coefficient of 0.803. In addition, we also found that the OA is 82.56% with a kappa coefficient of 0.816 in the season of autumn/winter.

**Table 6.** Confusion matrix of classification results of the study area, based on CART.

Referenced Category	Classified as							Total	PA (%)
	Vegetation	Plastic Film	Water	Bare Soil	Desert	Metal Rooftop	Cement Rooftop		
Vegetation	89	0	0	3	0	0	0	92	96.74
Plastic Film	1	147	0	13	0	11	9	181	81.21
Water	1	0	86	0	0	6	0	93	92.47
Bare Soil	8	13	0	148	12	0	12	193	76.68
Desert	0	8	0	18	96	0	1	123	78.05
Metal Rooftop	0	0	5	1	0	85	0	91	93.41
Cement Rooftop	0	8	0	18	5	0	104	135	77.03
Total	99	176	91	201	113	102	126	908	-
UA (%)	89.90	83.52	94.50	73.63	84.96	83.33	82.54	-	83.15

Overall accuracy (OA) = 83.15%. Kappa = 0.8030.

From the accuracy evaluation in Table 6, it is concluded that water has obtained the highest classification accuracy of both PA (92.47%) and UA (94.50%). Vegetation and metal rooftop observed good PA at 96.74% and 93.41%, respectively. The OA, however, declined to 89.90% and 93.33% for vegetation and metal rooftop, respectively. The bare soil observed the smallest classification accuracy both of PA (76.68%) and OA (73.63%), which is often

incorrectly classified as the desert or the plastic film, because their spectral reflectance are comparable (see Figure 4).

### 3.3.3. Land Cover Mapping of Dunkuotan Village

The automatic classification result is displayed in Figure 9 and is based on the decision tree algorithm. We can see that there are many areas of land with plastic film cover detected. The vegetation and bare soil were discriminated in accordance with the NDVI/EVI features. Moreover, the buildings with a metal rooftop were correctly identified, which are at an intersection or beside the main street of the village (at the center of Figure 9). Some of the buildings with a cement rooftop, however, were wrongly classified as the plastic film on the ground (at the bottom left of Figure 9) because of its extremely high spectral reflectance, which is close to that of the rooftop of cement.

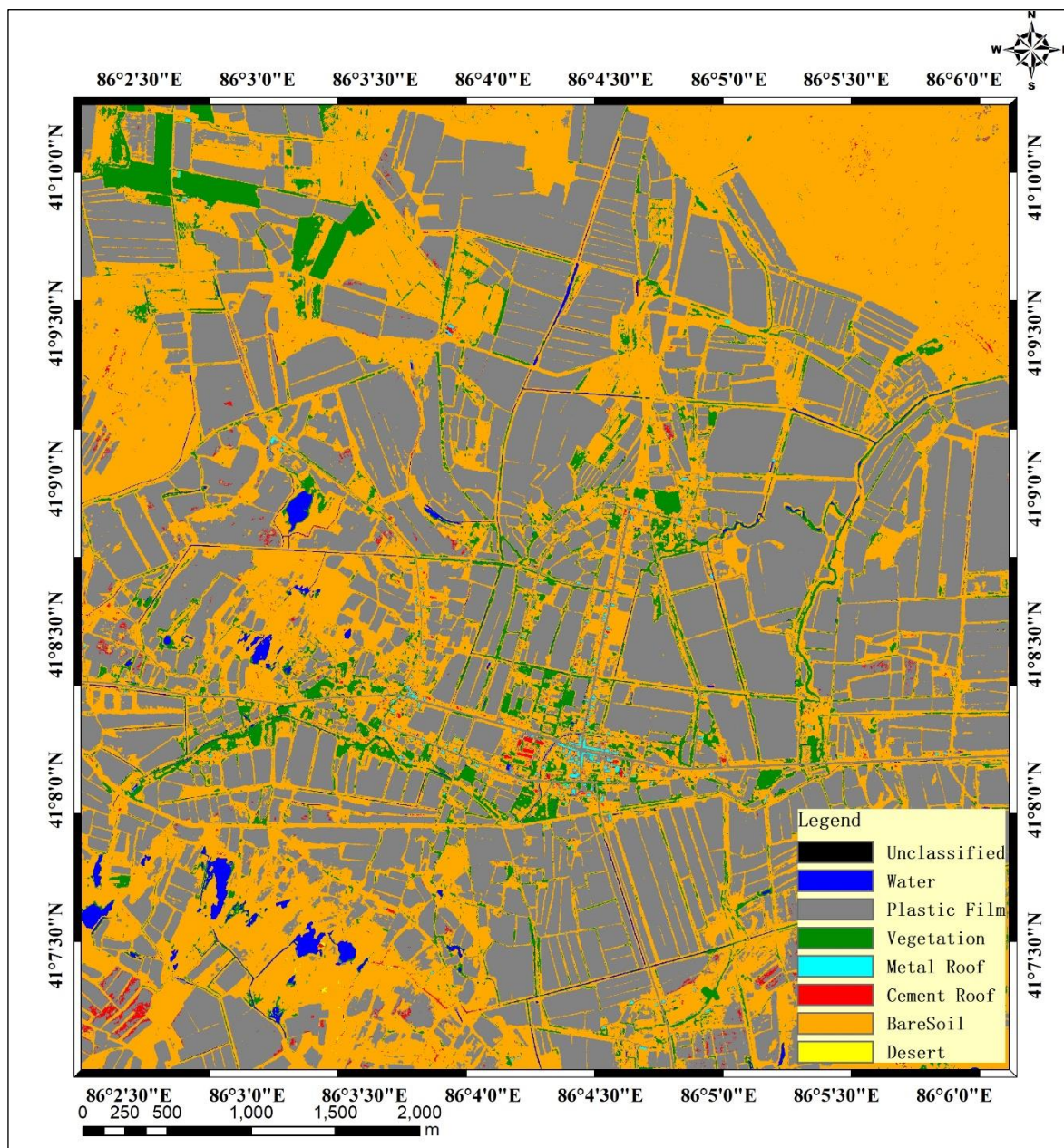


Figure 9. Land cover classification map of the center of Dunkuotan Village by decision tree.

### 3.4. Integrated Use of Optical and SAR Images for Land Cover Classification

The multispectral remote-sensing images, Gaofen-1/2 and Sentinel-2A/2B, for instance, and SAR images (e.g., GF-3, Sentinel-1A/B, etc.) are widely applied remote-sensing data sources in the classification of land cover and land use [36], especially for residence area identification [37]. The spectral indexes from optical remote-sensing images such as NDVI, NDWI and EVI can be served to discriminate between vegetated land and bare soil. The radar features of SAR remote-sensing images, on the other hand, are suitable to apply in the detection of buildings or residential regions because of the double-bounce effect in SAR images (see the bright spots in Figure 8). In addition, the optical images can be used in the classification of different types of rooftops on the basis of the difference of reflectance between the metal and the cement rooftop, according to the NDMRI index, which is proposed in this investigation. This is helpful when automatic workflow is applied to distinguish the inhabitation in rural districts from the commercial regional center. This scheme is extremely useful in the assessment of the sustainable development level among the regional cities in Western China. It can be concluded that the integrated use of indexes from optical and SAR images would enhance the robustness of classification for land cover and land use when a high-resolution remote-sensing application is concerned.

## 4. Conclusions

Gaofen satellites enjoy the advantages of high temporal and comparably high spatial resolution, where both optical and radar sensors are deployed. The GF-2 multispectral images and GF-3 SAR images were used in this investigation to analyze the characteristics of land cover in Yuli County, Xinjiang, China, by means of the CART algorithm of a decision tree. The overall classification accuracy of 83.15% with a kappa coefficient of 0.803 was observed for the study area. The vegetation, water, land with plastic film, bare soil, desert and buildings with metal or cement rooftops were classified accordingly. The DT-based classification for Gaofen satellite images proposed in this paper can be used in the reconnaissance and analysis of human activities in the sparsely populated zones of Western China to promote the effectiveness and accuracy of a routine administrative and supervised workflow.

**Author Contributions:** Conceptualization, R.C. and C.L.; methodology, C.L. and W.T.; image processing, J.Y. and X.M.; validation, C.L., W.T. and J.Y.; writing—original draft preparation, C.L. and W.T.; writing—review and editing, R.C. and C.L.; visualization, C.L. and W.T.; supervision, R.C.; funding acquisition, C.L. and W.T. All authors have read and agreed to the published version of the manuscript.

**Funding:** This research was funded by the China High-Resolution Earth Observation System (grant no. 01–Y30F05–9001–20/22), the National Key R&D Program of China (grant no. 2017YFC0822004) and the Civil Aerospace Pre-research Project of China (Key technologies for emergency observation and information support of domestic satellites, grant no. B0302).

**Institutional Review Board Statement:** Not applicable.

**Informed Consent Statement:** Not applicable.

**Data Availability Statement:** The Gaofen series satellite images can be found on the website of China Centre for Resources Satellite Data and Application (<https://data.cresda.cn/#/home>, accessed on 23 January 2023).

**Acknowledgments:** The authors thank the Remote Sensing Center of Public Security, People's Public Security University of China, for providing the Gaofen satellite images used in this investigation. The authors also thank three anonymous reviewers for their helpful comments and suggestions.

**Conflicts of Interest:** The authors declare no conflict of interest.

## Appendix A

All the abbreviations in this paper are listed below, in Table A1.

**Table A1.** The meaning of abbreviations used in this investigation.

Abbreviation	Full Term	Meaning
AWS	Amazon Web Services	The cloud platform that was developed by Amazon to handle remote-sensing big data.
CART	Classification and regression tree	One of the decision tree classification algorithms.
CCD	Charge coupled device	The optical sensors for remote-sensing image acquisition.
CHEOS	China's High-Resolution Earth Observation System	A Chinese earth observation system for the acquisition of high-resolution remote-sensing images.
CODE-DE	Copernicus Data and Exploitation Platform-DE	The cloud platform that was developed by Germany to handle remote-sensing big data.
DEM	Digital elevation model	A model that demonstrates the elevation of the Earth's surface.
DN	Digital number	The pixel value in a remote-sensing image.
DT	Decision tree	One of the machine-learning algorithms.
ENVI	Environment for visualizing images	The name of a type of software for remote-sensing image analysis, which was developed by Harris Corporation in Melbourne, Florida, USA.
EVI	Enhanced vegetation index	The index that demonstrates vegetation in optical remote-sensing images.
FLAASH	Fast Line-of-sight Atmospheric Analysis of Spectral Hypercubes	The atmospheric correction algorithm model.
GEE	Google Earth Engine	The platform used to process remote-sensing data online, which was developed by Google in the United States.
GF	GaoFen	The name of a Chinese high-resolution satellite.
GIS	geographic information system	The computer program used for the analysis of spatial information.
GPS	global navigation and positioning	The global navigation and positioning developed by the United States.
GTC	Geocoded terrain correction	One of the geo-correction methods for SAR remote-sensing images.
Kappa	Kappa coefficient	A value to quantitatively assess the accuracy of a classification.
MS	Multispectral	A type of optical remote-sensing image.
MVN	Mean value of NRCS	A statistic value that demonstrates the mean value of an NRCS.
NDMRI	Normalized difference metal rooftop index	The index that demonstrates metal rooftops in optical remote-sensing images.
NDVI	Normalized difference vegetation index	The index that demonstrates vegetation in optical remote-sensing images.
NDWI	Normalized difference water index	The index that demonstrates water in optical remote-sensing images.
NEX	NASA Earth Exchange	The cloud platform that was developed by NASA in the United States to handle remote-sensing big data.
NIR	Near infrared	The name for a specific spectrum.
NRCS	Normalized radar cross section	The parameter that is used to depict the capability of a target on the Earth to reflect the incidence of electromagnetic waves of radar.
OA	Overall accuracy	The statistical parameter that is used to demonstrate classification accuracy.
PA	Producer's accuracy	The statistical parameter that is used to demonstrate the classification accuracy.
PAN	Panchromatic	A type of optical remote-sensing image.
PIE	Pixel information expert	The cloud platform that was developed by PIESAT Group Inc. in China to handle remote-sensing big data.

Table A1. Cont.

Abbreviation	Full Term	Meaning
PIE-SAR	/	The name of a type of software for SAR image processing, which was developed by PIESAT Information Technology Co., Ltd., in China.
PMS	Panchromatic and multispectral	A type of optical remote-sensing sensor.
QPSI	Quad-Polarization Strip I	One of the image modes of GF-3 SAR sensors.
RPC	Rational polynomial coefficient	A commonly used geo-correction model.
RS	Remote sensing	A technique for spatial information acquisition.
SAR	Synthetic aperture radar	An active microwave sensor that is able to acquire high-resolution remote-sensing images.
SDN	Standard deviation of NRCS	A statistical value that demonstrates the variance of an NRCS.
UA	User's accuracy	The statistical parameter that is used to demonstrate classification accuracy.
UFS	Ultrafine strip	One of the image modes of GF-3 SAR sensors.
WFOV	Wide field of view	A type of optical remote-sensing sensor.

## References

- Tao, J.; Wu, W.; Liu, W.; Xu, M. Exploring the Spatio-Temporal Dynamics of Winter Rape on the Middle Reaches of Yangtze River Valley Using Time-Series MODIS Data. *Sustainability* **2020**, *12*, 466. [\[CrossRef\]](#)
- Yang, X.; Lin, L.; Zhang, Y.; Ye, T.; Chen, Q.; Jin, C.; Ye, G. Spatially Explicit Assessment of Social Vulnerability in Coastal China. *Sustainability* **2019**, *11*, 5075. [\[CrossRef\]](#)
- Huadong, G. Big Data, Big Science, Big Discovery—Review of CODATA Workshop on Big Data for International Scientific Programmes. *Bull. Chin. Acad. Sci.* **2014**, *29*, 500–506. [\[CrossRef\]](#)
- Fu, D.; Xiao, H.; Su, F.; Zhou, C.; Dong, J.; Zeng, Y.; Yan, K.; Li, S.; Wu, J.; Wu, W.; et al. Remote Sensing Cloud Computing Platform Development and Earth Science Application. *Natl. Remote Sens. Bull.* **2021**, *25*, 220–230. [\[CrossRef\]](#)
- Andries, A.; Murphy, R.J.; Morse, S.; Lynch, J. Earth Observation for Monitoring, Reporting, and Verification within Environmental Land Management Policy. *Sustainability* **2021**, *13*, 9105. [\[CrossRef\]](#)
- Amani, M.; Ghorbanian, A.; Ahmadi, S.A.; Kakooei, M.; Moghimi, A.; Mirmazloumi, S.M.; Moghaddam, S.H.A.; Mahdavi, S.; Ghahremanloo, M.; Parsian, S.; et al. Google Earth Engine Cloud Computing Platform for Remote Sensing Big Data Applications: A Comprehensive Review. *IEEE J. Sel. Top. Appl. Earth Obs. Remote Sens.* **2020**, *13*, 5326–5350. [\[CrossRef\]](#)
- Gorelick, N.; Hancher, M.; Dixon, M.; Ilyushchenko, S.; Thau, D.; Moore, R. Google Earth Engine: Planetary-Scale Geospatial Analysis for Everyone. *Remote Sens. Environ.* **2017**, *202*, 18–27. [\[CrossRef\]](#)
- Tamiminia, H.; Salehi, B.; Mahdianpari, M.; Quackenbush, L.; Adeli, S.; Brisco, B. Google Earth Engine for Geo-Big Data Applications: A Meta-Analysis and Systematic Review. *ISPRS J. Photogramm. Remote Sens.* **2020**, *164*, 152–170. [\[CrossRef\]](#)
- Padma, S.; Vidhya Lakshmi, S.; Prakash, R.; Srividhya, S.; Sivakumar, A.A.; Divyah, N.; Canales, C.; Saavedra Flores, E.I. Simulation of Land Use/Land Cover Dynamics Using Google Earth Data and QGIS: A Case Study on Outer Ring Road, Southern India. *Sustainability* **2022**, *14*, 16373. [\[CrossRef\]](#)
- Huadong, G. A Project on Big Earth Data Science Engineering. *Bull. Chin. Acad. Sci.* **2018**, *33*, 818–824. [\[CrossRef\]](#)
- Feng, Q.; Chen, B.; Li, G.; Yao, X.; Gao, B.; Zhang, L. A Review for Sample Datasets of Remote Sensing Imagery. *Natl. Remote Sens. Bull.* **2022**, *26*, 589–605. [\[CrossRef\]](#)
- Zhang, B. Remotely Sensed Big Data Era and Intelligent Information Extraction. *Geomat. Inf. Sci. Wuhan Univ.* **2018**, *43*, 1861–1871. [\[CrossRef\]](#)
- Chen, L.; Letu, H.; Fan, M.; Shang, H.; Tao, J.; Wu, L.; Zhang, Y.; Yu, C.; Gu, J.; Zhang, N.; et al. An Introduction to the Chinese High-Resolution Earth Observation System: Gaofen-1~7 Civilian Satellites. *J. Remote Sens.* **2022**, *2022*, 9769536. [\[CrossRef\]](#)
- Wang, C.; Qiu, X.; Liu, H.; Li, D.; Zhao, K.; Wang, L. Damaged Buildings Recognition of Post-Earthquake High-Resolution Remote Sensing Images Based on Feature Space and Decision Tree Optimization. *Comput. Sci. Inf. Syst.* **2020**, *17*, 619–646. [\[CrossRef\]](#)
- Tariq, A.; Yan, J.; Gagnon, A.S.; Riaz Khan, M.; Mumtaz, F. Mapping of Cropland, Cropping Patterns and Crop Types by Combining Optical Remote Sensing Images with Decision Tree Classifier and Random Forest. *Geo-Spat. Inf. Sci.* **2022**, *25*, 1–19. [\[CrossRef\]](#)

16. Maxwell, A.E.; Warner, T.A.; Fang, F. Implementation of Machine-Learning Classification in Remote Sensing: An Applied Review. *Int. J. Remote Sens.* **2018**, *39*, 2784–2817. [[CrossRef](#)]
17. Breiman, L.; Friedman, J.H.; Olshen, R.A.; Stone, C.J. *Classification and Regression Trees*; Wadsworth and Brooks: Belmont, CA, USA, 1984.
18. Qu, L.; Chen, Z.; Li, M. CART-RF Classification with Multifilter for Monitoring Land Use Changes Based on MODIS Time-Series Data: A Case Study from Jiangsu Province, China. *Sustainability* **2019**, *11*, 5657. [[CrossRef](#)]
19. Patil, V.C.; Al-Gaadi, K.A.; Madugundu, R.; Tola, E.K.; Zeyada, A.M.; Marey, S.; Biradar, C.M. CART and IDC-Based Classification of Irrigated Agricultural Fields Using Multi-Source Satellite Data. *Geocarto Int.* **2018**, *33*, 70–88. [[CrossRef](#)]
20. Rodriguez-Galiano, V.F.; Chica-Olmo, M.; Abarca-Hernandez, F.; Atkinson, P.M.; Jeganathan, C. Random Forest Classification of Mediterranean Land Cover Using Multi-Seasonal Imagery and Multi-Seasonal Texture. *Remote Sens. Environ.* **2012**, *121*, 93–107. [[CrossRef](#)]
21. Ruiz Hernandez, I.E.; Shi, W. A Random Forests Classification Method for Urban Land-Use Mapping Integrating Spatial Metrics and Texture Analysis. *Int. J. Remote Sens.* **2018**, *39*, 1175–1198. [[CrossRef](#)]
22. Pal, M.; Mather, P.M. An Assessment of the Effectiveness of Decision Tree Methods for Land Cover Classification. *Remote Sens. Environ.* **2003**, *86*, 554–565. [[CrossRef](#)]
23. Tie, B.; Huang, F.; Tao, J.; Lu, J.; Qiu, D. A Parallel and Optimization Approach for Land-Surface Temperature Retrieval on a Windows-Based PC Cluster. *Sustainability* **2018**, *10*, 621. [[CrossRef](#)]
24. Liu, D.; Liao, T.; Sun, H.; Ren, F. Research Progress and Development Direction of Chinese Remote Sensing Software: Taking PIE as an Example. *J. Image Graph.* **2021**, *26*, 1169–1178. [[CrossRef](#)]
25. Hou, J.; Ye, M. Effects of Dynamic Changes of Soil Moisture and Salinity on Plant Community in the Bosten Lake Basin. *Sustainability* **2022**, *14*, 14081. [[CrossRef](#)]
26. Loukika, K.N.; Keesara, V.R.; Sridhar, V. Analysis of Land Use and Land Cover Using Machine Learning Algorithms on Google Earth Engine for Munneru River Basin, India. *Sustainability* **2021**, *13*, 13758. [[CrossRef](#)]
27. Shi, L.; Li, P.; Yang, J.; Zhang, L.; Ding, X.; Zhao, L. Co-Polarization Channel Imbalance Phase Estimation by Corner-Reflector-like Targets. *ISPRS J. Photogramm. Remote Sens.* **2019**, *147*, 255–266. [[CrossRef](#)]
28. Bertsimas, D.; Dunn, J. Optimal Classification Trees. *Mach. Learn.* **2017**, *106*, 1039–1082. [[CrossRef](#)]
29. Hellesen, T.; Matikainen, L. An Object-Based Approach for Mapping Shrub and Tree Cover on Grassland Habitats by Use of LiDAR and CIR Orthoimages. *Remote Sens.* **2013**, *5*, 558–583. [[CrossRef](#)]
30. Basheer, S.; Wang, X.; Farooque, A.A.; Nawaz, R.A.; Liu, K.; Adekanmbi, T.; Liu, S. Comparison of Land Use Land Cover Classifiers Using Different Satellite Imagery and Machine Learning Techniques. *Remote Sens.* **2022**, *14*, 4978. [[CrossRef](#)]
31. Ren, B.; Ma, S.; Hou, B.; Hong, D.; Chanussot, J.; Wang, J.; Jiao, L. A Dual-Stream High Resolution Network: Deep Fusion of GF-2 and GF-3 Data for Land Cover Classification. *Int. J. Appl. Earth Obs. Geoinf.* **2022**, *112*, 102896. [[CrossRef](#)]
32. Shao, Y.; Fan, X.; Liu, H.; Xiao, J.; Ross, S.; Brisco, B.; Brown, R.; Staples, G. Rice Monitoring and Production Estimation Using Multitemporal RADARSAT. *Remote Sens. Environ.* **2001**, *76*, 310–325. [[CrossRef](#)]
33. Gade, M.; Alpers, W.; Melsheimer, C.; Tanck, G. Classification of Sediments on Exposed Tidal Flats in the German Bight Using Multi-Frequency Radar Data. *Remote Sens. Environ.* **2008**, *112*, 1603–1613. [[CrossRef](#)]
34. Tian, W.; Bian, X.; Shao, Y.; Zhang, Z. On the Detection of Oil Spill with China’s HJ-1C SAR Image. *Aquat. Procedia* **2015**, *3*, 144–150. [[CrossRef](#)]
35. Cui, Z.; Dang, S.; Cao, Z.; Wang, S.; Liu, N. SAR Target Recognition in Large Scene Images via Region-Based Convolutional Neural Networks. *Remote Sens.* **2018**, *10*, 776. [[CrossRef](#)]
36. Yang, Z.; Zhang, H.; Lyu, X.; Du, W. Improving Typical Urban Land-Use Classification with Active-Passive Remote Sensing and Multi-Attention Modules Hybrid Network: A Case Study of Qibin District, Henan, China. *Sustainability* **2022**, *14*, 14723. [[CrossRef](#)]
37. Lun, N.S.; Chaudhary, S.; Ninsawat, S. Assessment of Machine Learning Methods for Urban Types Classification Using Integrated SAR and Optical Images in Nonthaburi, Thailand. *Sustainability* **2023**, *15*, 1051. [[CrossRef](#)]

**Disclaimer/Publisher’s Note:** The statements, opinions and data contained in all publications are solely those of the individual author(s) and contributor(s) and not of MDPI and/or the editor(s). MDPI and/or the editor(s) disclaim responsibility for any injury to people or property resulting from any ideas, methods, instructions or products referred to in the content.